Editors' Suggestion

Clean quantum point contacts in an InAs quantum well grown on a lattice-mismatched InP substrate

Connie L. Hsueh,[1,2,3,*] Praveen Sriram,[1,2,3,*] Tiantian Wang,[4,5] Candice Thomas,[4,5] Geoffrey Gardner,[5,6] Marc A. Kastner,[2,7,8] Michael J. Manfra,[4,5,6,9,10] and David Goldhaber-Gordon[2,8,†]

[1]*Department of Applied Physics, Stanford University, Stanford, California 94305, USA*
[2]*Stanford Institute for Materials and Energy Sciences, SLAC National Accelerator Laboratory, Menlo Park, California 94025, USA*
[3]*Geballe Laboratory for Advanced Materials, Stanford University, Stanford, California 94305, USA*
[4]*Department of Physics and Astronomy, Purdue University, West Lafayette, Indiana 47907, USA*
[5]*Birck Nanotechnology Center, West Lafayette, Indiana 47907, USA*
[6]*Microsoft Quantum Lab Purdue, Purdue University, West Lafayette, Indiana 47907, USA*
[7]*Department of Physics, Massachusetts Institute of Technology, Cambridge, Massachusetts 02139, USA*
[8]*Department of Physics, Stanford University, Stanford, California 94305, USA*
[9]*School of Electrical and Computer Engineering, Purdue University, West Lafayette, Indiana 47907, USA*
[10]*School of Materials Engineering, Purdue University, West Lafayette, Indiana 47907, USA*

(Received 15 February 2022; accepted 8 April 2022; published 6 May 2022)

Strong spin-orbit coupling, the resulting large g factor, and small effective mass make InAs an attractive material platform for inducing topological superconductivity. The surface Fermi level pinning in the conduction band enables highly transparent ohmic contact without excessive doping. We investigate electrostatically defined quantum point contacts (QPCs) in a deep-well InAs two-dimensional electron gas. Despite the 3.3% lattice mismatch between the InAs quantum well and the InP substrate, we report clean QPCs with up to eight pronounced quantized conductance plateaus at zero magnetic field. Source-drain dc bias spectroscopy reveals a harmonic confinement potential with a nearly 5 meV subband spacing. We find a many-body exchange interaction enhancement for the out-of-plane g factor $|g^*_\perp| = 27 \pm 1$, whereas the in-plane g factor is isotropic $|g^*_x| = |g^*_y| = 12 \pm 2$, close to the bulk value for InAs.

DOI: 10.1103/PhysRevB.105.195303

I. INTRODUCTION

A quantum point contact (QPC) is a ballistic quasi-one-dimensional constriction with a tunable conductance, quantized in multiples of e^2/h [1]. First demonstrated in GaAs/$Al_xGa_{1-x}As$ two-dimensional electron gases (2DEGs) over three decades ago [2,3], QPCs have been incorporated into mesoscale quantum devices for tunnel spectroscopy [4], quantum dots [5], charge sensors [6,7], electron injectors [8], spin polarizers [9], electronic beam splitters [10], and more. However, demonstrations of clean QPCs in InAs heterostructures remain far fewer.

InAs-based nanostructures have come under a renewed spotlight as a potential platform for proximity-induced topological superconductivity [11,12]. InAs has a small effective mass, large spin-orbit coupling, and surface Fermi level pinning [13]. Proximitized by an s-wave superconductor and exposed to a magnetic field, a one-dimensional InAs nanostructure should host Majorana zero modes at its ends [14–16]. This makes InAs-based systems an enticing platform for observing and manipulating Majorana zero modes, toward possible eventual topological quantum information processing [17–20]. InAs 2DEGs can be top-down patterned, offering a scaling advantage over directly grown nanowires for creating complex geometries and for scaling to large numbers of devices [12,21]. The small effective mass $m^* = 0.03m_e$ [22,23] in InAs quantum wells (QWs) results in a weak temperature and bias dependence of resistivity, making it easier to decouple the background 2DEG in transport measurements of the QPC. Furthermore, a single valley degree of freedom with large bulk g factor ~12-15 makes InAs QWs a promising material platform for fast control of spin qubits [26–28] and quantum simulation of many-body phases [29,30]. Clean QPCs with smoothly tunable transitions are a key building block for integrating InAs quantum dot arrays in quantum simulators and processors.

We report the investigation of quantized conductance and magnetotransport properties of a narrow gate-defined constriction, fabricated in a buried InAs 2DEG grown by molecular beam epitaxy (MBE) on an InP substrate. The 3.3% lattice mismatch [13] between InAs and InP leads to a compressive strain on the quantum well and introduces dislocation defects; we demonstrate that, despite this, our QPCs are the cleanest amongst the handful of reported works in etched and gate-defined constrictions in InAs and InAs/InGaAs QWs [9,31–34]. The more closely lattice-matched substrate choice of GaSb has been plagued for decades with trivial edge conduction at mesa edges [35–38], which complicates interpretation of transport measurements. Though purely gate-defined nanostructures have recently allowed circumventing

*These authors contributed equally to this work.
†goldhaber-gordon@stanford.edu

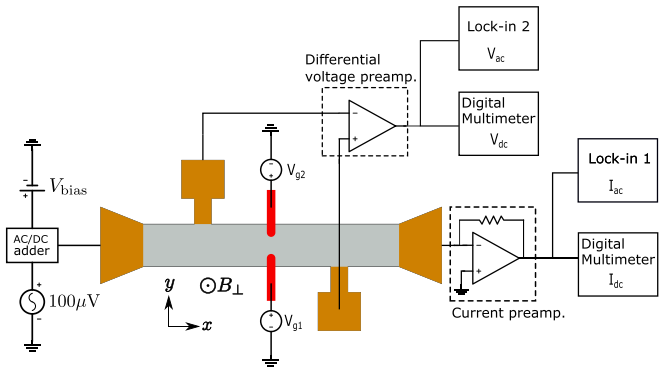

FIG. 1. Schematic representation of the measurement setup. The quantum point contact (QPC) is defined on a 5-μm-wide mesa (gray) with Ti/Au ohmic contacts (yellow). The QPC gates (red) are biased with dc voltage sources $V_{g1,g2}$. The Hall bar is biased with a 100 μV low-frequency (<20 Hz) ac excitation and a dc bias V_{bias}. The ac and dc components of the diagonal voltage drop across the QPC are measured after differential amplification by a lock-in amplifier V_{ac} and digital voltmeter V_{dc}. The voltage probes have a 60 μm horizontal separation. A current preamplifier provides a virtual ground at the drain, and a lock-in amplifier and digital ammeter are used to measure the ac and dc components of the drain current, I_{ac} and I_{dc}, respectively.

this [33,39], InP has superior insulating properties compared to GaSb, simplifying the fabrication and operation of quantum devices. The QPC featured in this paper shows eight pronounced quantized conductance plateaus with a harmonic subband spacing near 5 meV. The spin-split conductance plateaus in an applied magnetic field let us extract an isotropic in-plane effective g factor $|g_x^*| = |g_y^*| = 12 \pm 2$ and an exchange interaction-enhanced out-of-plane $|g_\perp^*| = 27 \pm 1$. Our work supports the integration of QPCs into quantum dots and other nanostructures.

II. DEVICE FABRICATION AND EXPERIMENT SETUP

The device was fabricated on a heterostructure grown by MBE on a semi-insulating InP (100) substrate; the growth is characterized in detail in Ref. [40] (sample B). The layer sequence is shown in the cross-sectional schematic Fig. S1(a) in the Supplemental Material (SM) [23]. The active region consists of a 4 nm InAs QW sandwiched between 10.5 nm of $In_{0.75}Ga_{0.25}As$ layers. A 900 nm step-graded buffer of $In_xAl_{1-x}As$ helps overcome the native lattice mismatch between InP and the quantum well, and a 120 nm $In_{0.75}Al_{0.25}As$ top barrier moves the active region away from the surface for increased mobility.

Carriers originating from deep-level donor states in the $In_{0.75}Al_{0.25}As$ layers populate the 2DEG formed in the InAs QW [41,42]. The 2DEG has a mobility $\mu = 4.55 \times 10^5$ cm^2/V s at an electron density $n_s = 4.34 \times 10^{11}$ cm^{-2} as measured in a 5-μm-wide Hall bar at $T = 1.5$ K, corresponding to a mean-free path of $l_{mf} = 4.9$ μm. Owing to suppressed alloy and InGaAs/InAs interface scattering in our buried deep-well heterostructure, the mobility is amongst the highest reported for InAs QWs and is limited by unintentional background impurities and native charged point defects [23,40].

Our samples are first processed with standard electron beam lithography and wet etching to define an extended Hall barlike mesa with an area of 5 μm × 60 μm between voltage probes. The etch depth is 300 nm, extending into the buffer layer to achieve electrical isolation. To improve surface and edge contact, Ti/Au ohmic contacts are deposited after a light, additional wet etch and *in situ* Ar mill. A 35-nm HfO_2 dielectric layer is added by atomic layer deposition at 150 °C. Finally, Ti/Au gate electrodes are deposited in multiple steps to form pairs of split gates of width 100 nm ($\ll l_{mf}$) and lithographically designed separations in the range 175–475 nm. The QPC highlighted in this work has separation 325 nm and data from additional QPCs are included in the SM [23].

The measurements reported here are performed at $T = 1.5$ K in a pumped He-4 cryostat, over multiple cooldowns. A low frequency (<20 Hz) ac excitation of 100 μV rms is applied between the source (S) and drain (D) contacts on the extended Hall bar. The current at the drain, I_{ac}, and diagonal voltage drop across the QPC, V_{ac}, are measured using standard low-frequency lock-in techniques. A schematic of the measurement configuration is shown in Fig. 1. The conductance through the QPC is $G = (V_{ac}/I_{ac} - R_s)^{-1}$, where R_s is the gate-independent 2DEG resistance between the voltage probes.

III. RESULTS AND DISCUSSION

A. Conductance quantization

Negatively biasing the split gates with a voltage around −1.5 V depletes the 2DEG directly underneath, forming a quasi-one-dimensional constriction. Upon further biasing, Fig. 2(a) clearly shows eight plateaus in G at even multiples of the conductance quantum e^2/h as a function of symmetric gate voltage ($V_{g1} = V_{g2} = V_g$), signifying ballistic transport through the spin-degenerate one-dimensional subbands in the gate-defined constriction, before completely pinching off around −2.9 V. Beyond pinch-off, the current is below the noise floor of the preamplifier $I_{pinch\text{-}off} < 1$ pA, implying a pinch-off resistance $R_{pinch\text{-}off} > 10^8\Omega$. The appearance of eight quantized conductance plateaus reveals the pristine nature of the constriction defined by the QPC, and exceeds previous reports [33,34]. This is compatible with the lithographic split-gate separation $W_{litho} = 325$ nm and Fermi wavelength $\lambda_F = 36.8$ nm in the 2DEG. The constriction is well described by a saddle-point model in the few-mode limit ($G \leqslant 8e^2/h$), as shown in the SM [23] and the references [43,44] therein. Immediately after cooling the sample, we often observe that pinch-off and other conductance features in G vs V_g gradually drift toward more negative gate voltages. This could be due to the dynamics of charge traps within the dielectric layer. After a few days, conductance features in repeated voltage sweeps become reproducible to within a 1 mV relative voltage shift. For consistency, we report data measured with V_g swept upwards, although once the potential drift stabilizes no significant difference is observed between the two sweep directions.

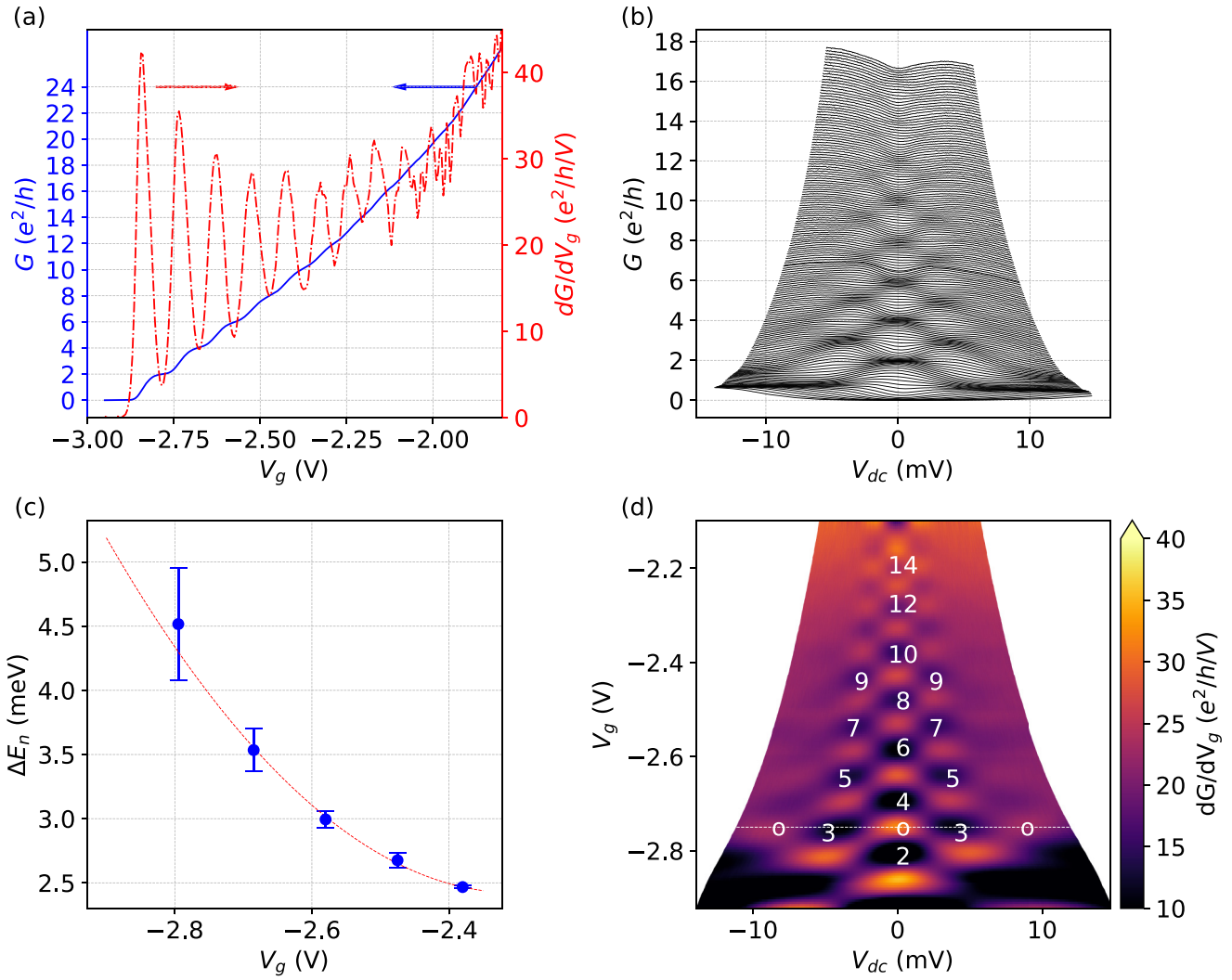

FIG. 2. (a) Four-terminal conductance G (blue solid line) and transconductance dG/dV_g (red broken line) through the QPC as the constriction width and local carrier density are modulated by the voltage applied to the split gates. Quantized conductance plateaus at even-integer multiples of e^2/h are observed. The large number of quantized plateaus visible is an indication of the pristine nature of the QPC. A series resistance $R_s = 380\Omega$ has been subtracted to adjust for the 2DEG resistance between the probes. dc bias spectroscopy showing the (b) conductance as a function of V_{dc} and (d) transconductance as a function of V_g and V_{dc}. Each trace in (b) corresponds to a fixed $V_g \in [-2.92, -2.1]$ V with a step size of 5 mV. A bunching of traces is observed at even multiples of e^2/h around zero bias and at odd multiples at finite bias. The dark regions in (d) correspond to the labeled conductance plateaus in units of e^2/h. The bright diamond-shaped stripes of finite transconductance correspond to transitions between the plateaus. A triplet of transconductance maxima, illustrated by the white circles and a dashed horizontal line at $V_g = -2.735$ V, highlights the harmonicity of the confinement potential. (c) QPC subband spacing plotted as a function of V_g for the first five subbands. Sweeping the QPC voltages up from pinch-off reduces the curvature of the confinement potential, decreasing the subband spacing. The subband spacings phenomenologically show a quadratic dependence on V_g.

B. Finite-bias spectroscopy

The level spectrum of the constriction can be probed by applying a dc bias voltage V_{bias} across the source and drain electrodes of the device. The dc voltage drop across the QPC, V_{dc}, is obtained by subtracting the voltage drop across the bare 2DEG: $V_{dc} = V_{meas} - I_{dc} \times R_s$, where V_{meas} is the four-terminal dc voltage difference measured across the QPC, I_{dc} is the dc current through the Hall bar, and $R_s = 380\Omega$ is a series resistance arising from the mesa 2DEG resistance. Figure 2(b) plots G as a function of V_{dc}, where each trace corresponds to a particular V_g, as the QPC is opened from pinch-off. A bunching of traces is observed at conductance plateaus, which are even multiples of e^2/h at low bias and odd multiples at high bias. The transconductance dG/dV_g is shown in Fig. 2(d) as a function of V_{dc} and V_g, with the dark regions corresponding to conductance plateaus and bright regions representing transitions.

The extent of the transconductance diamond for $G = n \times 2e^2/h$ along V_{dc} is a common measure [45] of the energy spacing $\Delta E_n(V_g^*)$ of QPC subbands $\{n, n+1\}$ at the gate voltage V_g^* corresponding to the diamond end points. Opening the QPC from pinch-off decreases the curvature of the confinement potential, decreasing the subband spacing with V_g as shown in Fig. 2(c). The harmonicity of the confinement

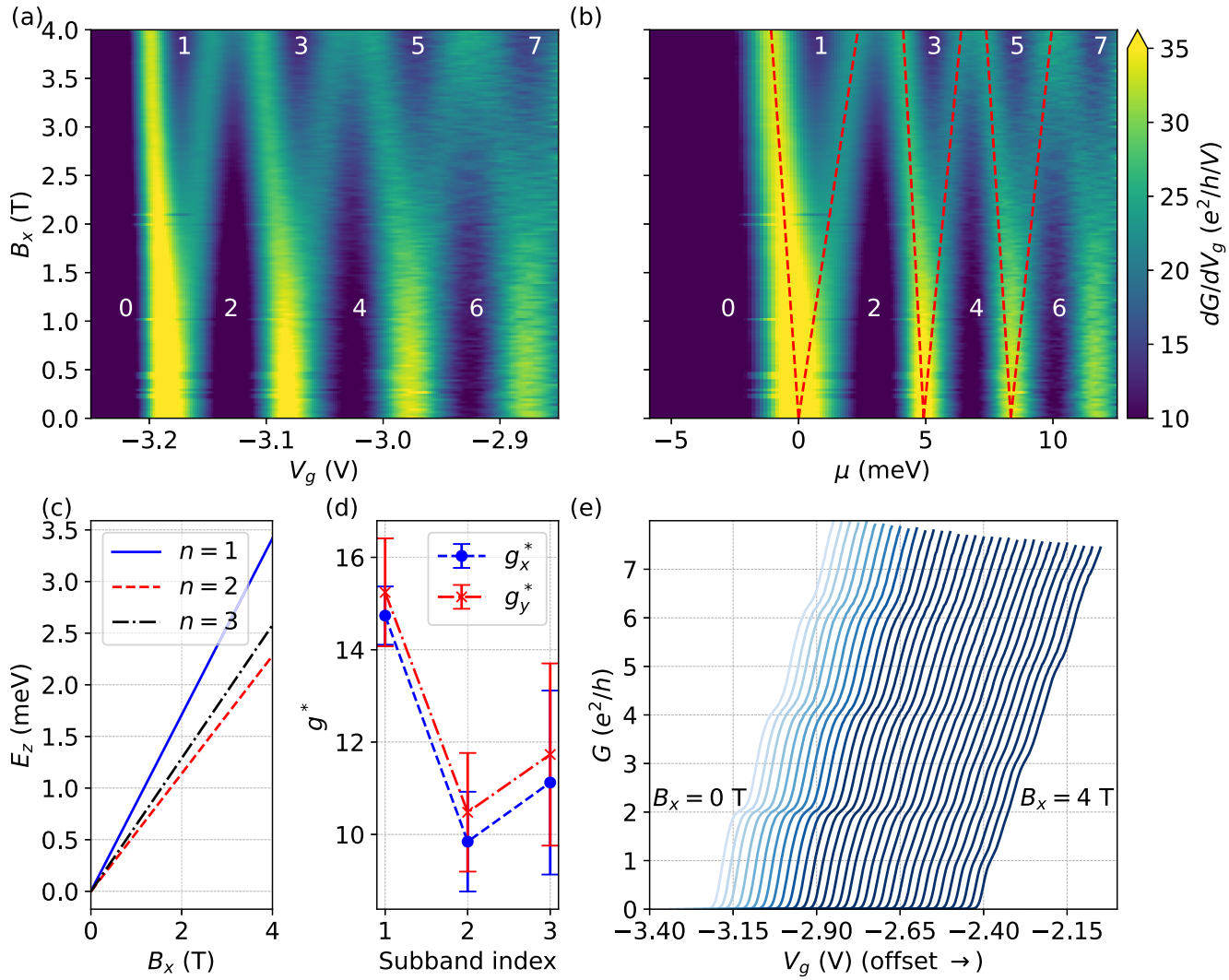

FIG. 3. In-plane magnetic field spectroscopy showing (a) transconductance dG/dV_g as a function of QPC gate voltage V_g and a magnetic field B_x applied in the plane of the sample and parallel to the transport direction and (b) as a function of chemical potential μ estimated from the capacitive lever arm (see the SM [23]). The dark regions correspond to conductance plateaus labeled in units of e^2/h. The transitions between conductance plateaus are visible as bright regions. The appearance of additional dark regions at high B_x ($\gtrsim$3 T) is a signature of a Zeeman-induced spin splitting of the subbands. (c) The Zeeman energy for the first three subbands, extracted from a linear fit to the spin-split transitions [red dotted lines in (b)]. (d) The effective in-plane g factor parallel (g_x^*) and perpendicular (g_y^*) to the transport direction estimated from the slopes of the Zeeman energy in (c) for the first three subbands. Within the error bars, the in-plane effective g factor is isotropic and close to the bulk value for InAs $|g| = 13$. (e) Conductance as a function of V_g at various fixed B_x. The traces in (e) are offset along the horizontal axis for clarity and display a progressive development of conductance plateaus at $1e^2/h$, $3e^2/h$, and $5e^2/h$.

potential in a particular gate voltage range can be probed by considering a triplet of transconductance maxima circled in Fig. 2(d). Since they occur at approximately the same gate voltage, we infer $\Delta E_1 \simeq \Delta E_2$ [45]. Similar horizontal lines can be drawn connecting diamond vertices at higher conductances, implying a harmonic confinement potential, albeit a function of V_g .

Approximating the lateral confinement as a harmonic potential with a gate voltage-dependent angular frequency $\omega_0(V_g)$, the length scale $L_n(V_g^*)$ of the transverse real-space extent of the subbands at $V_g = V_g^*$ can be estimated as

$$\tfrac{1}{2}m^*\omega_0^2 L_n^2 = \hbar\omega_0\left(n - \tfrac{1}{2}\right), \quad (1)$$

where $m^* = 0.03m_e$ [22,23] is the effective mass and m_e is the bare electron mass. Taking $\hbar\omega_0(V_g^*) = \Delta E_n(V_g^*)$ for the nth subband spacing as determined above, the corresponding length scales can be estimated as $L_1 = 22.7 \pm 0.9$ nm, $L_2 = 45.8 \pm 1.1$ nm, and $L_3 = 64.5 \pm 0.8$ nm for the first three subbands, consistent with expectations from the lithographic width $W_{\text{litho}} = 325$ nm $\gg L_n$.

C. In-plane magnetic field

Spin-resolved transport through the QPC can be studied by applying a magnetic field B_x in the plane of the sample and parallel to the transport direction. Figure 3(a) shows the transconductance dG/dV_g as a function of B_x and V_g,

as the gate voltage is swept up from pinch-off. The dark, diamond-shaped regions at low B_x ($\lesssim$2 T) correspond to the spin-degenerate even-integer conductance plateaus. At higher applied B_x, the spin splitting by the Zeeman effect dominates over the subband linewidths, resulting in the appearance of odd plateaus as additional dark regions interleaved with the spin-degenerate diamonds. Conductance traces as a function of V_g for different B_x are shown in Fig. 3(e). As expected, conductance plateaus at $1e^2/h$ and $3e^2/h$ emerge as B_x is increased and the width of the even-integer plateaus correspondingly decreases.

Figure 3(b) elucidates the spin-split subband spectrum by translating V_g to a chemical potential μ, using the split-gate lever arm $\alpha = d\mu/dV_g$ extracted from Fig. 2(d) (see the SM [23] for details on the conversion). A linear fit to the transconductance maxima for each spin-split subband pair is used to extract the Zeeman energy E_Z as a function of B_x, as depicted in Fig. 3(c). These linear fits were constrained to intersect at $B_x = 0$ for each spin-split subband pair. The in-plane g factor extracted from the slope of the Zeeman energy is shown in Fig. 3(d), with error estimates based on fitting parameter variances. Figure 3(d) also shows the in-plane g factor measured in a magnetic field B_y in-plane but perpendicular to the direction of transport, revealing negligible anisotropy $g_x^* \simeq g_y^*$ (see the SM [23]). This is consistent with previous measurements in (In,Ga)As [46], InSb [47], and n-type GaAs [48] QPCs. The isotropic in-plane g factor points to a weak Rashba spin-orbit coupling in the constriction [49]. The absence of intentional dopants and the symmetric $In_{0.75}Ga_{0.25}As$ barrier structure in the QW stack result in a symmetric 2DEG confinement potential. As revealed by self-consistent Schrödinger-Poisson simulations, the QW hosts an electron wave function with symmetric tails in the barrier regions [see Fig. S1(b)] in the SM [23]). This inversion symmetry of QW in the growth direction [001] leads to the isotropic effective g factor for in-plane magnetic fields [50]. Furthermore, the estimated in-plane g factor $|g^*_{x,y}|$ for the first three subbands $= \{15 \pm 1, 10 \pm 1, 11 \pm 2\}$ is typical for bulk InAs ($g_{\mathrm{InAs}} \simeq -13$ [51,52]), with an enhancement for the $n = 1$ subband in agreement with theoretical predictions based on exchange interactions [53,54].

D. Out-of-plane magnetic field

As a next step in investigating the QPC, we study the effect of electrostatic confinement on magnetic subbands by applying a magnetic field $B_\perp$ perpendicular to the plane of the sample. The conductance G as V_g is swept up from pinch-off for $B_\perp \in [0, 4]$ T is shown in Fig. 4(a). The cyclotron energy of the electrons, $\hbar\omega_c = \hbar eB_\perp/m^*$ where e is the electron charge, adds in quadrature to the QPC confinement energy. The resultant magnetoelectric subbands have a spacing that initially grows quadratically with field ($\omega_y \gg \omega_c$) before transitioning into a linear increase as they line up with the 2DEG Landau levels for $2r_c < W_{\mathrm{qpc}}$ [56], where $r_c = \hbar k_F/eB_\perp$ is the cyclotron radius of the classical electron trajectory in the 2DEG, $k_F = \sqrt{2\pi n_s}$ is the Fermi wave number in the 2DEG, and $W_{\mathrm{qpc}}(V_g)$ is the gate voltage-dependent constriction width (see Sec. S6 in the SM [23]). The increase in subband spacing and suppression of backscattering through the Hall bar with $B_\perp$ results in broader and more pronounced conductance plateaus. Furthermore, the Zeeman effect of the applied field lifts spin degeneracy and results in the emergence of odd-integer conductance plateaus. Because of thermal ($k_BT \sim$ 130 μeV) and disorder broadening in our measurements, we observe spin-split plateaus only at $B_\perp \gtrsim 2$ T (red trace).

Figure 4(b) depicts the transconductance dG/dV_g as a function of $B_\perp$ and V_g. The dark regions correspond to conductance plateaus, separated by bright features which represent the transitions between the plateaus. The transconductance has a local maximum whenever a subband edge is resonant with the source and/or drain chemical potential. Given that the confinement is described by a V_g-dependent harmonic potential, the magnetoelectric subbands can be described by the Beenakker and van Houten model [55]

$$E_{n,\pm} = E_0 + (n - 1/2)\hbar\sqrt{\omega_y^2(V_g) + \omega_c^2} \pm \tfrac{1}{2}g^*_\perp\mu_B B_\perp, \quad (2)$$

where $n = 1, 2, \ldots$ is the spin-degenerate subband index, $\pm$ labels the spin-split subband with spin oriented antiparallel (parallel) to $B_\perp$, E_0 is the energy offset of the conduction band edge, $\hbar\omega_y = \Delta E_n$ is the V_g-dependent QPC subband spacing at $B_\perp = 0$ T [see Fig. 2(d)], and $g^*_\perp$ is the effective out-of-plane g factor. The white dashed curve in Fig. 4(b) marks the contour $W_{\mathrm{qpc}}(V_g) = 2r_c$. An agreement to Eq. (2), when translated to gate voltage, in the low-field regime ($B_\perp < 2\hbar k_F/eW_{\mathrm{qpc}}$) for $n \in \{1, 2, 3\}$ is shown as red dotted lines in Fig. 4(b). The spin-degenerate part of Eq. (2) used for the $n = 3$ subband edge spin splitting is not well observed for $W_{\mathrm{qpc}} < 2r_c$.

The Zeeman energy can be measured by performing finite-bias spectroscopy of the QPC as a function of $B_\perp$. In a setup identical to Sec. III B, the QPC conductance is measured as a function of an applied dc voltage at a fixed $B_\perp$. Figure 4(c) shows the transconductance as a function of the dc voltage drop across the QPC V_{dc} and V_g around the $G = 1e^2/h$ plateau at $B_\perp = 2.85$ T. The dark highlighted region corresponds to the $1e^2/h$ plateau, the extent of which along V_{dc} corresponds to the Zeeman energy $E_Z = g^*_\perp\mu_B B_\perp = 4$ meV. Measured as a function of $B_\perp$, Fig. 4(d) shows the Zeeman energy evolution with field which fits a straight line constrained to pass through the origin, for $|g^*_\perp| = 27 \pm 1$. The uncertainty in ascertaining the boundaries of the $G = 1e^2/h$ plateau, as evinced by broadened transconductance peaks in Fig. 4(c), results in large error bars for the Zeeman energies, defined as the width corresponding to 99% relative peak height. This can also be seen from the broad transconductance peaks in the $B_\perp \in [2, 4]$ T region of Fig. 4(b). Nevertheless, we can report a twofold enhancement of the out-of-plane g factor compared to the in-plane and bulk InAs value $g^*_\perp/g^*_{x,y} \approx 2$.

The reduced symmetry in quasi-2D heterostructures, as compared to the bulk, introduces anisotropy between $g^*_\perp$ and $g^*_{x,y}$ [50]. Furthermore, as previously measured [46] and analyzed [49] for (In,Ga)As QPCs, the orbital effect of the out-of-plane field strengthens many-body exchange interactions in the 2DEG, resulting in an enhanced $g^*_\perp$. The depopulation of consecutive spin-split Landau levels with $B_\perp$ leads to an oscillatory exchange enhancement, with local maxima at odd filling factors [57–59]. Sadofyev *et al.* [58] measured an enhanced out-of-plane g factor $\simeq 60$ at high

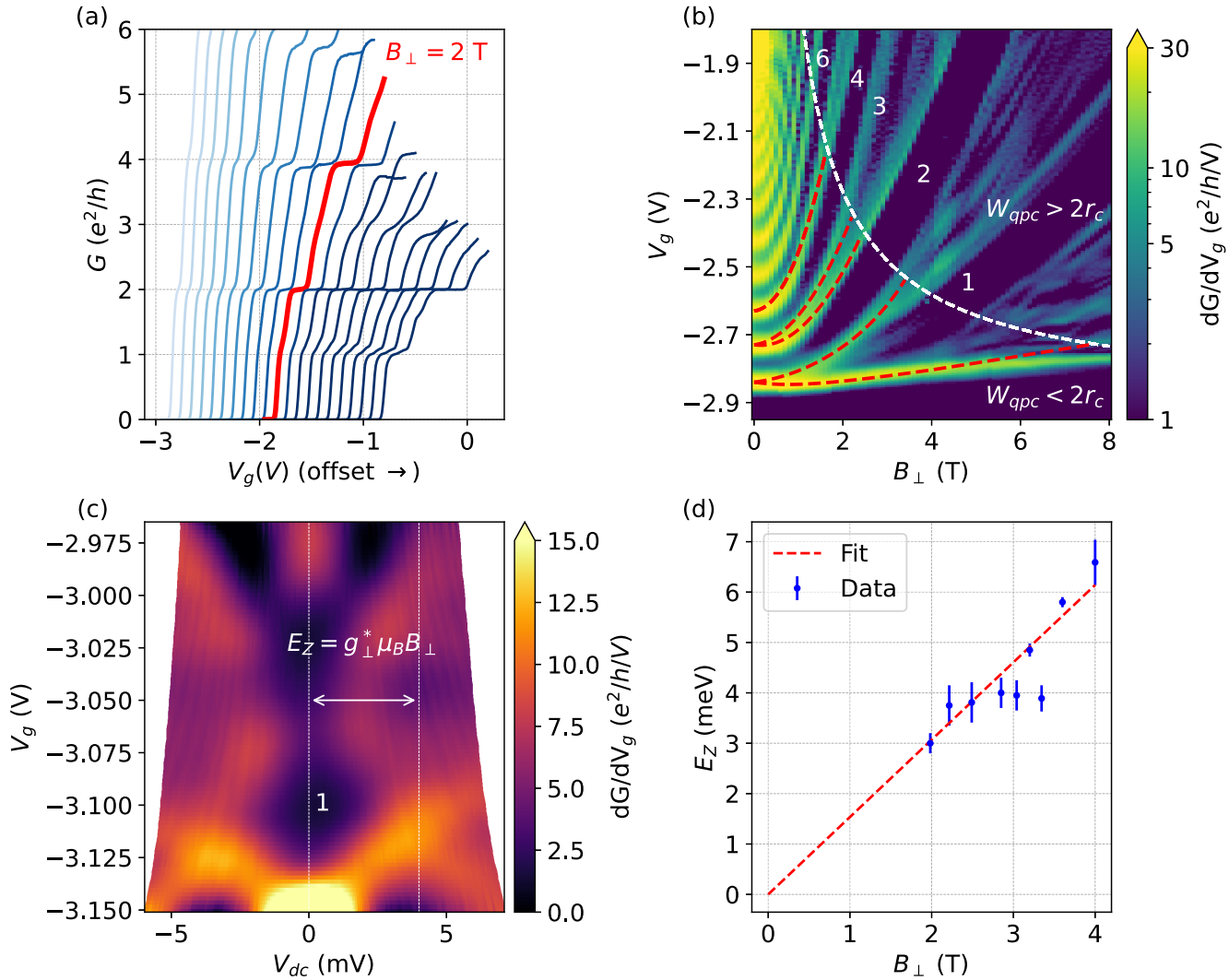

FIG. 4. (a) Conductance G of the QPC as a function of V_g for a series of out-of-plane magnetic fields. The curves are offset along the horizontal axis for clarity. Above $B_\perp = 2$ T (bold red trace), odd-integer conductance plateaus emerge. (b) Transconductance dG/dV_g as a function of QPC gate voltage V_g and a magnetic field $B_\perp$ applied out of plane of the sample. The dark regions correspond to conductance plateaus labeled in units of e^2/h. The transitions between conductance plateaus are visible as bright regions and illustrate the magnetoelectric subband energy evolution with field. The white dashed curve marks the subband transition to 2DEG Landau levels, based on the gate dependent constriction width $W_{qpc}(V_g)$ and cyclotron radius r_c. The red dashed lines show agreement with a model by Beenakker and van Houten [55] in the low-field regime $W_{qpc} < 2r_c$. (c) Transconductance as a function of V_{dc} and V_g at $B_\perp = 2.85$ T. The white dashed lines highlight the extent of the $1e^2/h$ conductance plateau diamond along the V_{dc} axis, a measure of the Zeeman energy E_Z. (d) The $B_\perp$ dependence of the Zeeman energy, as extracted from the $1e^2/h$ transconductance diamond size, similar to (c). The linear fit, weighted by inverse E_Z variances, shows an effective out-of-plane g factor $|g^*_\perp| \sim 27 \pm 1$.

fields in InAs/AlSb QWs. Similar measurements for $g^*_\perp$ in our QW reveal an enhanced 2DEG g factor $\simeq 30$ in the $B_\perp \in [2, 4]$ T field range (see the SM [23]). Consequently, we attribute the enhanced splitting of the QPC subband [Figs. 4(c) and 4(d)] to many-body exchange interactions in the 2DEG, rather than 1D confinement effects due to the constriction.

E. Shifting the confinement potential

By applying an asymmetric voltage bias to the QPC split gates, we can laterally shift the position of the confining potential in real space. This serves as a spatial map of localized disorder or other potential fluctuations which may increase backscattering in the channel or create accidental quantum dots [60]. Tuning the two gate voltages independently, the transconductance with respect to the fast sweep axis V_{g2} is shown in Fig. 5. The bright features correspond to transitions between conductance plateaus and they appear consistently smooth across the entire range. Resonances caused by localized disorder would appear as additional gate voltage-dependent lines in this map; the absence of such features here suggests a clean, defect-free channel within this range. Tuning the gate asymmetry to avoid spurious resonances is a common technique in QPC operation—not needing it here will significantly simplify the operation of devices with larger numbers of gates, where cross-capacitances

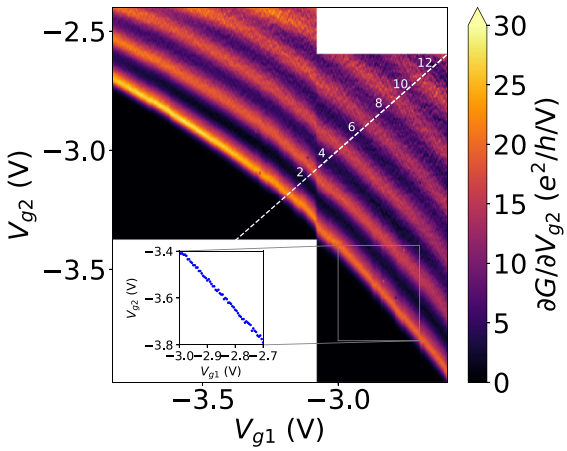

FIG. 5. Transconductance with respect to fast sweep axis V_{g2}, as a function of the two gate voltages, with data taken in two sweeps separated by a few hours. The discontinuity at $V_{g1} = -3.08$ V corresponds to drift in the QPC conductance between sweeps (see the SM [23] for discussion on stability). The dark regions correspond to conductance plateaus, labeled in units of e^2/h, while the bright regions indicate transitions between them. In the shown gate voltage range, at least four conductance plateaus are visible. The white dotted line marks the trajectory of the symmetric gate sweep (V_{g1} and V_{g2}) used in this work. The inset shows a fit to the first transconductance maxima in the $V_{g1} \in [-3, -2.7]$ V and $V_{g2} \in [-3.8, -3.4]$ V range, with discontinuities (at $V_{g1} = -2.84$ V, for example) arising from a drift in the QPC conductance between traces along the slow sweep axis V_{g1}.

must be diligently accounted for. The blue dots in the inset show a fit to the first transconductance peak in the $V_{g1} \in [-3, -2.7]$ V and $V_{g2} \in [-3.8, -3.4]$ V range. The discontinuities in the fit are due to a drift in the QPC conductance between traces along the slow sweep axis V_{g1}. We additionally note that we do not observe signatures of the 0.7 anomaly or of half-quantized plateaus at zero magnetic field in this QPC, though they have been reported previously in similar structures [31,32,34]. This raises the question of the universality of such features in heterostructures of this type.

IV. CONCLUSION

We have presented the fabrication and characterization of a QPC in an InAs-based deep quantum well which displays remarkable cleanliness despite the lattice-mismatched InP substrate. Transport through the QPC is smoothly quantized at zero and finite B field, and bias spectroscopy reveals a harmonic confining potential with large subband spacing of near 5 meV. We find an isotropic in-plane g factor $|g^*_{x,y}| = 12 \pm 2$ and an out-of-plane g factor $|g^*_{\perp}| = 27 \pm 1$.

This study supports the integration of QPCs as tunable tunnel barriers, charge sensors [6,7], or mode collimators [8,10] into more complex InAs-based two-dimensional quantum devices such as quantum dots. This is a critical building block toward investigations in spintronics, spin qubits, and hybrid superconductor-semiconductor topological physics.

The data that support the findings of this study are available from the corresponding author upon request.

ACKNOWLEDGMENTS

We thank W. Pouse, E. Mikheev, J. Williams, M. Pendharkar, A. C. C. Drachmann, K. Ensslin, T. Ihn, Z. Lei, H. Sahasrabudhe, R. Rahman, and F. Pierre for their scientific insights and suggestions. Measurement and analysis were supported by the U.S. Department of Energy (DOE), Office of Science, Basic Energy Sciences (BES), under Contract No. DE-AC02-76SF00515. Growth and characterization of heterostructures was supported by Microsoft Quantum. C.L.H. acknowledges support from the National Science Foundation (NSF) and Stanford Graduate Fellowship (SGF). Part of this work was performed at the Stanford Nano Shared Facilities (SNSF), supported by the National Science Foundation under Award No. ECCS-2026822.

[1] H. van Houten and C. Beenakker, Phys. Today **49**(7), 22 (1996).
[2] B. J. van Wees, H. van Houten, C. W. J. Beenakker, J. G. Williamson, L. P. Kouwenhoven, D. van der Marel, and C. T. Foxon, Phys. Rev. Lett. **60**, 848 (1988).
[3] D. A. Wharam, T. J. Thornton, R. Newbury, M. Pepper, H. Ahmed, J. E. F. Frost, D. G. Hasko, D. C. Peacock, D. A. Ritchie, and G. A. C. Jones, J. Phys. C **21**, L209 (1988).
[4] M. Kjaergaard, F. Nichele, H. J. Suominen, M. P. Nowak, M. Wimmer, A. R. Akhmerov, J. A. Folk, K. Flensberg, J. Shabani, C. J. Palmstrøm *et al.*, Nat. Commun. **7**, 12841 (2016).
[5] U. Meirav, M. A. Kastner, and S. J. Wind, Phys. Rev. Lett. **65**, 771 (1990).
[6] J. M. Elzerman, R. Hanson, L. H. Willems van Beveren, B. Witkamp, L. M. K. Vandersypen, and L. P. Kouwenhoven, Nature (London) **430**, 431 (2004).
[7] D. Reilly, C. Marcus, M. Hanson, and A. Gossard, Appl. Phys. Lett. **91**, 162101 (2007).
[8] H. van Houten, B. Van Wees, J. Mooij, C. Beenakker, J. Williamson, and C. Foxon, Europhys. Lett. **5**, 721 (1988).
[9] P. Debray, S. M. S. Rahman, J. Wan, R. S. Newrock, M. Cahay, A. T. Ngo, S. E. Ulloa, S. T. Herbert, M. Muhammad, and M. Johnson, Nat. Nanotechnol. **4**, 759 (2009).
[10] Y. Ji, Y. Chung, D. Sprinzak, M. Heiblum, D. Mahalu, and H. Shtrikman, Nature (London) **422**, 415 (2003).
[11] M. T. Deng, S. Vaitiekenas, E. B. Hansen, J. Danon, M. Leijnse, K. Flensberg, J. Nygård, P. Krogstrup, and C. M. Marcus, Science **354**, 1557 (2016).
[12] A. Fornieri, A. M. Whiticar, F. Setiawan, E. Portolés, A. C. C. Drachmann, A. Keselman, S. Gronin, C. Thomas, T. Wang, R. Kallaher, G. C. Gardner, E. Berg, M. J. Manfra, A. Stern, C. M. Marcus, and F. Nichele, Nature (London) **569**, 89 (2019).
[13] I. Vurgaftman, J. R. Meyer, and L. R. Ram-Mohan, J. Appl. Phys. **89**, 5815 (2001).
[14] Y. Oreg, G. Refael, and F. von Oppen, Phys. Rev. Lett. **105**, 177002 (2010).

[15] R. M. Lutchyn, J. D. Sau, and S. Das Sarma, Phys. Rev. Lett. **105**, 077001 (2010).

[16] R. M. Lutchyn, E. P. A. M. Bakkers, L. P. Kouwenhoven, P. Krogstrup, C. M. Marcus, and Y. Oreg, Nat. Rev. Mater. **3**, 52 (2018).

[17] D. Aasen, M. Hell, R. V. Mishmash, A. Higginbotham, J. Danon, M. Leijnse, T. S. Jespersen, J. A. Folk, C. M. Marcus, K. Flensberg, and J. Alicea, Phys. Rev. X **6**, 031016 (2016).

[18] J. Alicea, Y. Oreg, G. Refael, F. von Oppen, and M. P. A. Fisher, Nat. Phys. **7**, 412 (2011).

[19] T. Hyart, B. van Heck, I. C. Fulga, M. Burrello, A. R. Akhmerov, and C. W. J. Beenakker, Phys. Rev. B **88**, 035121 (2013).

[20] T. Karzig, C. Knapp, R. M. Lutchyn, P. Bonderson, M. B. Hastings, C. Nayak, J. Alicea, K. Flensberg, S. Plugge, Y. Oreg, C. M. Marcus, and M. H. Freedman, Phys. Rev. B **95**, 235305 (2017).

[21] J. Shabani, M. Kjaergaard, H. J. Suominen, Y. Kim, F. Nichele, K. Pakrouski, T. Stankevic, R. M. Lutchyn, P. Krogstrup, R. Feidenhans'l, S. Kraemer, C. Nayak, M. Troyer, C. M. Marcus, and C. J. Palmstrøm, Phys. Rev. B **93**, 155402 (2016).

[22] J. Shabani, S. Das Sarma, and C. J. Palmstrøm, Phys. Rev. B **90**, 161303(R) (2014).

[23] See Supplemental Material at http://link.aps.org/supplemental/10.1103/PhysRevB.105.195303 for details on the (1) InAs heterostructure stack, which includes Refs. [24,25], (2) fabrication, instrumentation, and measurement details, (3) effective mass estimation, (4) saddle-point model, (5) gate voltage dependence of constriction width, (6) lever arm, (7) in-plane magnetic field perpendicular to transport direction, (8) out-of-plane 2DEG g factor, and (9) notes on stability and reproducibility.

[24] S. Steiger, M. Povolotskyi, H.-H. Park, T. Kubis, and G. Klimeck, IEEE Trans. Nanotechnol. **10**, 1464 (2011).

[25] S. Das Sarma and E. H. Hwang, Phys. Rev. B **88**, 035439 (2013).

[26] C. Mittag, J. V. Koski, M. Karalic, C. Thomas, A. Tuaz, A. T. Hatke, G. C. Gardner, M. J. Manfra, J. Danon, T. Ihn, and K. Ensslin, PRX Quantum **2**, 010321 (2021).

[27] K. D. Petersson, L. W. McFaul, M. D. Schroer, M. Jung, J. M. Taylor, A. A. Houck, and J. R. Petta, Nature (London) **490**, 380 (2012).

[28] S. Nadj-Perge, S. M. Frolov, E. P. A. M. Bakkers, and L. P. Kouwenhoven, Nature (London) **468**, 1084 (2010).

[29] T. Hensgens, T. Fujita, L. Janssen, X. Li, C. J. Van Diepen, C. Reichl, W. Wegscheider, S. Das Sarma, and L. M. K. Vandersypen, Nature (London) **548**, 70 (2017).

[30] J. P. Dehollain, U. Mukhopadhyay, V. P. Michal, Y. Wang, B. Wunsch, C. Reichl, W. Wegscheider, M. S. Rudner, E. Demler, and L. M. K. Vandersypen, Nature (London) **579**, 528 (2020).

[31] J. Shabani, A. McFadden, B. Shojaei, and C. Palmstrøm, Appl. Phys. Lett. **105**, 262105 (2014).

[32] S. Matsuo, H. Kamata, S. Baba, R. S. Deacon, J. Shabani, C. J. Palmstrøm, and S. Tarucha, Phys. Rev. B **96**, 201404(R) (2017).

[33] C. Mittag, M. Karalic, Z. Lei, C. Thomas, A. Tuaz, A. T. Hatke, G. C. Gardner, M. J. Manfra, T. Ihn, and K. Ensslin, Phys. Rev. B **100**, 075422 (2019).

[34] J. S. Lee, B. Shojaei, M. Pendharkar, A. P. McFadden, Y. Kim, H. J. Suominen, M. Kjaergaard, F. Nichele, H. Zhang, C. M. Marcus *et al.*, Nano Lett. **19**, 3083 (2019).

[35] S. Mueller, C. Mittag, T. Tschirky, C. Charpentier, W. Wegscheider, K. Ensslin, and T. Ihn, Phys. Rev. B **96**, 075406 (2017).

[36] F. K. de Vries, T. Timmerman, V. P. Ostroukh, J. van Veen, A. J. A. Beukman, F. Qu, M. Wimmer, B.-M. Nguyen, A. A. Kiselev, W. Yi, M. Sokolich, M. J. Manfra, C. M. Marcus, and L. P. Kouwenhoven, Phys. Rev. Lett. **120**, 047702 (2018).

[37] F. Nichele, H. J. Suominen, M. Kjaergaard, C. M. Marcus, E. Sajadi, J. A. Folk, F. Qu, A. J. A. Beukman, F. K. de Vries, J. van Veen, S. Nadj-Perge, L. P. Kouwenhoven, B.-M. Nguyen, A. A. Kiselev, W. Yi, M. Sokolich, M. J. Manfra, E. M. Spanton, and K. A. Moler, New J. Phys. **18**, 083005 (2016).

[38] C. Thomas, A. T. Hatke, A. Tuaz, R. Kallaher, T. Wu, T. Wang, R. E. Diaz, G. C. Gardner, M. A. Capano, and M. J. Manfra, Phys. Rev. Materials **2**, 104602 (2018).

[39] C. Mittag, M. Karalic, Z. Lei, T. Tschirky, W. Wegscheider, T. Ihn, and K. Ensslin, Appl. Phys. Lett. **113**, 262103 (2018).

[40] A. T. Hatke, T. Wang, C. Thomas, G. C. Gardner, and M. J. Manfra, Appl. Phys. Lett. **111**, 142106 (2017).

[41] F. Capotondi, G. Biasiol, I. Vobornik, L. Sorba, F. Giazotto, A. Cavallini, and B. Fraboni, J. Vac. Sci. Technol. B **22**, 702 (2004).

[42] J. K. Luo, H. Thomas, S. A. Clark, and R. H. Williams, J. Appl. Phys. **74**, 6726 (1993).

[43] M. Geier, J. Freudenfeld, J. T. Silva, V. Umansky, D. Reuter, A. D. Wieck, P. W. Brouwer, and S. Ludwig, Phys. Rev. B **101**, 165429 (2020).

[44] S. Laux, D. Frank, and F. Stern, Surf. Sci. **196**, 101 (1988).

[45] C. Rössler, S. Baer, E. de Wiljes, P.-L. Ardelt, T. Ihn, K. Ensslin, C. Reichl, and W. Wegscheider, New J. Phys. **13**, 113006 (2011).

[46] T. P. Martin, A. Szorkovszky, A. P. Micolich, A. R. Hamilton, C. A. Marlow, R. P. Taylor, H. Linke, and H. Q. Xu, Phys. Rev. B **81**, 041303(R) (2010).

[47] F. Qu, J. van Veen, F. K. de Vries, A. J. A. Beukman, M. Wimmer, W. Yi, A. A. Kiselev, B.-M. Nguyen, M. Sokolich, M. J. Manfra, F. Nichele, C. M. Marcus, and L. P. Kouwenhoven, Nano Lett. **16**, 7509 (2016).

[48] K. J. Thomas, J. T. Nicholls, M. Y. Simmons, M. Pepper, D. R. Mace, and D. A. Ritchie, Phys. Rev. Lett. **77**, 135 (1996).

[49] K. Kolasiński, A. Mreńca-Kolasińska, and B. Szafran, Phys. Rev. B **93**, 035304 (2016).

[50] R. Winkler, Introduction, in *Spin-Orbit Coupling Effects in Two-Dimensional Electron and Hole Systems* (Springer, Berlin, Heidelberg, 2003), pp. 1–8.

[51] C. R. Pidgeon, D. L. Mitchell, and R. N. Brown, Phys. Rev. **154**, 737 (1967).

[52] J. Konopka, Phys. Lett. A **26**, 29 (1967).

[53] T. Ando and Y. Uemura, J. Phys. Soc. Jpn. **37**, 1044 (1974).

[54] C.-K. Wang and K.-F. Berggren, Phys. Rev. B **54**, R14257 (1996).

[55] C. Beenakker and H. van Houten, in *Semiconductor Heterostructures and Nanostructures*, Solid State Physics, edited by H. Ehrenreich and D. Turnbull (Academic Press, New York, 1991), Vol. 44, pp. 1–228.

[56] C. Beenakker, H. van Houten, and B. van Wees, Superlattices Microstruct. **5**, 127 (1989).

[57] R. J. Nicholas, R. J. Haug, K. v. Klitzing, and G. Weimann, Phys. Rev. B **37**, 1294 (1988).

[58] Y. G. Sadofyev, A. Ramamoorthy, B. Naser, J. P. Bird, S. R. Johnson, and Y.-H. Zhang, Appl. Phys. Lett. **81**, 1833 (2002).

[59] K. S. Cho, T.-Y. Huang, C.-P. Huang, Y.-H. Chiu, C.-T. Liang, Y. F. Chen, and I. Lo, J. Appl. Phys. **96**, 7370 (2004).

[60] J. G. Williamson, C. E. Timmering, C. J. P. M. Harmans, J. J. Harris, and C. T. Foxon, Phys. Rev. B **42**, 7675 (1990).